

Calvin University

Calvin Digital Commons

University Faculty Publications and Creative Works

University Faculty Scholarship

11-1-2020

Re-examining the Radial Distributions of M13 Multiple Populations

Jason P. Smolinski
Calvin University

Willem B. Hoogendam
Calvin University

Alex J. Van Kooten
Calvin University

Peyton Benac
Harvard-Smithsonian Center for Astrophysics

Follow this and additional works at: https://digitalcommons.calvin.edu/calvin_facultypubs



Part of the [Optics Commons](#)

Recommended Citation

Smolinski, Jason P.; Hoogendam, Willem B.; Van Kooten, Alex J.; and Benac, Peyton, "Re-examining the Radial Distributions of M13 Multiple Populations" (2020). *University Faculty Publications and Creative Works*. 173.

https://digitalcommons.calvin.edu/calvin_facultypubs/173

This Article is brought to you for free and open access by the University Faculty Scholarship at Calvin Digital Commons. It has been accepted for inclusion in University Faculty Publications and Creative Works by an authorized administrator of Calvin Digital Commons. For more information, please contact digitalcommons@calvin.edu.



Re-examining the Radial Distributions of M13 Multiple Populations

Jason P. Smolinski¹ , Willem B. Hoogendam¹, Alex J. Van Kooten¹ , Peyton Benac² , and Zachary J. Bruce

¹Department of Physics & Astronomy, Calvin University, Grand Rapids, MI 49546, USA; js85@calvin.edu

²Harvard-Smithsonian Center for Astrophysics, Cambridge, MA 02139, USA

Received 2020 July 22; revised 2020 September 4; accepted 2020 September 7; published 2020 October 15

Abstract

We seek to resolve the tension in the literature regarding the presence of radially segregated multiple populations in the Galactic globular cluster M13. Previous studies of this nearby cluster have presented discordant results about the degree of dynamical mixing in M13's inner region. Using ground-based (*UBVI*) photometry, we show that cumulative radial distributions of stars on the blue and red sides of the red giant branch are statistically identical. Interestingly, these results are obtained using data from large-aperture, ground-based telescopes as well as a more modestly sized instrument, and both are in agreement with previous work done using Hubble Space Telescope and Strömrgren photometry. Results are derived using the $C_{U,B,I}$ index, shown to be sensitive to compositional differences. We discuss our conclusions that the chemically distinct populations within M13 may be dynamically mixed in the context of published results from simulations.

Unified Astronomy Thesaurus concepts: Globular star clusters (656); Red giant branch (1368); Hertzsprung Russell diagram (725); Broad band photometry (184); Dynamical evolution (421)

1. Introduction

Spectroscopic analysis of stars in Galactic globular clusters (GCs) has produced a paradigm for cluster evolution that includes the presence or formation of multiple stellar populations (MSPs). Such MSPs are chemically different in light elements (e.g., He, C, N, O, Na) in ways that are typically explained in the context of advanced nucleosynthetic sequences occurring within a first generation of stars, where nuclear processed material is brought to the surface and dispersed into the intracluster medium via slow winds, rapid rotation, or some other mechanism. According to this model, gas enriched in particular elements like N and Na and depleted in elements like C and O coalesces in the cluster core and forms a second, enriched generation of stars. While this model does not neatly explain every GC's observed abundance pattern (e.g., Bastian et al. 2015) or ratio of enriched to unenriched stars (Carretta et al. 2010), it generally does a sufficiently adequate job of qualitatively explaining the vast majority of Milky Way GCs studied to date that it has become the current leading model describing GC chemical evolution.

While the study of GC MSPs has largely been done using spectroscopy, given its advantage in identifying true chemical differences, photometric studies have lent themselves to expanding the study of GCs in this area as well. Using photometry to distinguish stellar subpopulations requires high resolution and signal-to-noise ratio (S/N), and this is most easily accomplished using space-based or large ground-based observatories. Indeed, a series of work done by Piotto et al. (2015) handily demonstrated the utility of the Hubble Space Telescope (hereafter HST) in identifying these subpopulations from high-precision photometry. Yong et al. (2008) demonstrated that ground-based photometry in intermediate-width Strömrgren filters could be successfully used in distinguishing populations of stars within GCs by identifying subtle color differences among red giant branch (RGB) stars resulting from variations in atomic and/or molecular absorption within these passbands.

Broadband Johnson *U* and *B* filters were used in conjunction with spectroscopy by Marino et al. (2008) to show that differences in ($U - B$) color corresponded to differences in O, Na, and N abundances, where relatively Na-poor/CN-weak stars lie on the blue side of the RGB and relatively Na-rich/CN-strong (enriched) stars lie on the red side, a result of the presence of several CN and NH absorption features in the *U* passband. Kravtsov et al. (2010a, 2010b) and Kravtsov et al. (2011) further illustrated the distinction between these subpopulations on the RGB by revealing radial distribution differences between red RGB and blue RGB stars, where the red RGB stars in their studies were reported to be more centrally concentrated. This finding was further emphasized by Lardo et al. (2011, hereafter referred to as L11), who looked at a collection of Sloan Digital Sky Survey (SDSS; in particular Abazajian et al. 2009) GCs and identified radial segregation in most of them using SDSS photometry alone. It remains a contested point whether segregated radial distributions are perhaps fairly common or relatively uncommon (e.g., Larsen et al. 2015; Lim et al. 2016). Vanderbeke et al. (2015), for example, reported that 80% of their sample of 48 GCs appeared to be well mixed.

Results for individual clusters are not always in agreement. The comprehensive study by L11 of GCs in the SDSS database suggested that the Galactic GC M13 has a centralized concentration of enriched stars when examined over a radial range of 0.7–6.7 half-light radii (r_h). This is seemingly at odds with the study by Savino et al. (2018, hereafter referred to as S18), which used HST data and ground-based Strömrgren data from the Isaac Newton Telescope (hereafter INT) out to a radial distance of 6.5 r_h and reported M13 to be well mixed over the entire radial range. Given the angular size and visual brightness of M13, this cluster is of fundamental value to the study of dynamical mixing among chemically distinct subpopulations because it should be among the best opportunities to obtain meaningful and reliable results using a large sample of stars that are well resolved inside 2 r_h . In short, getting this cluster right is important for the validation of dynamical simulations. Furthermore, if the limiting factors in such work

are resolution and S/N, combining the crowded-field analysis power of the DAOPHOT photometry suite (Stetson 1987; Stetson & Harris 1988) with a significant amount of exposure time could potentially open up this space to sub-1-m telescopes as well.

In this study we describe a procedure for attempting to distinguish stellar subpopulations in Galactic GCs using a modestly sized telescope, and the application of that procedure to the Galactic GC M13. In Section 2 we detail our data acquisition and reduction steps, and the membership selection procedure is described in Section 3. The application of our procedure to M13 is detailed in Section 4, where we also describe the rigorous testing we performed to give us confidence in our data and our procedure. In Section 5 we tackle the question of why previous results from L11 and S18 appear to be contradictory, and then we compare the result of this study with dynamical predictions in Section 6. Finally, we discuss our conclusions in Section 7.

2. Observations and Data Reduction

Our dataset for M13 was obtained over multiple nights between 2016 June and 2019 June using the Calvin University 0.4 m robotic observatory, located in Rehoboth, New Mexico. The data were collected using an SBIG ST-10XE thermoelectrically cooled CCD with a plate scale of $1''.31$ per 2×2 -binned pixel, producing a field of view of roughly $24' \times 16'$. Images were taken in Johnson-Cousins *UBVI*. The total effective exposure times in the (*U*, *B*, *V*, *I*) filters were (63,600, 23,400, 8,910, 8,820) seconds, respectively. All images were reduced via standard procedures using the MaxIm DL image acquisition, reduction, and analysis software package. All images passing an adopted seeing quality threshold of ≤ 3.9 arcsec (3.0 pixels) FWHM in *VI* and ≤ 4.7 arcsec (3.6 pixels) FWHM in *UB* were weight-averaged in IRAF,³ where the weighting factors were a function of each image's background sky noise. This resulted in a single master image in each filter with $S/N \geq 100$ along the portion of the RGB we targeted. The seeing threshold values were selected based on what was determined to be optimal seeing for our instrument and site.

Because of the crowded nature of these fields, the DAOPHOT/ALLSTAR photometry suite (Stetson 1987; Stetson & Harris 1988) was employed to obtain instrumental photometry for stars in each master image. Briefly, this procedure involved carefully constructing a point-spread function (PSF) from a group of ~ 50 selected stars within each master image and using this PSF to fit and subtract detected stars in an interactive fashion, where each iteration completely refitted the original image using a list of all stars detected up to that point. The process of searching for and fitting stars in each image was iterated 3–4 times to obtain photometry that had acceptably low uncertainties. DAOMASTER produced our final cross-matched multiband catalog. DAOPHOT provides a *sharp* statistic that quantifies the detection as being particularly point-like or extended, where the parameter is defined to be zero for point-like detections. Following the lead of S18 and others, we adopted a cutoff value of $|sharp| \leq 0.3$ to exclude extended sources and artifacts.

³ IRAF is distributed by the National Optical Astronomy Observatory, which is operated by the Association of Universities for Research in Astronomy (AURA) under a cooperative agreement with the National Science Foundation.

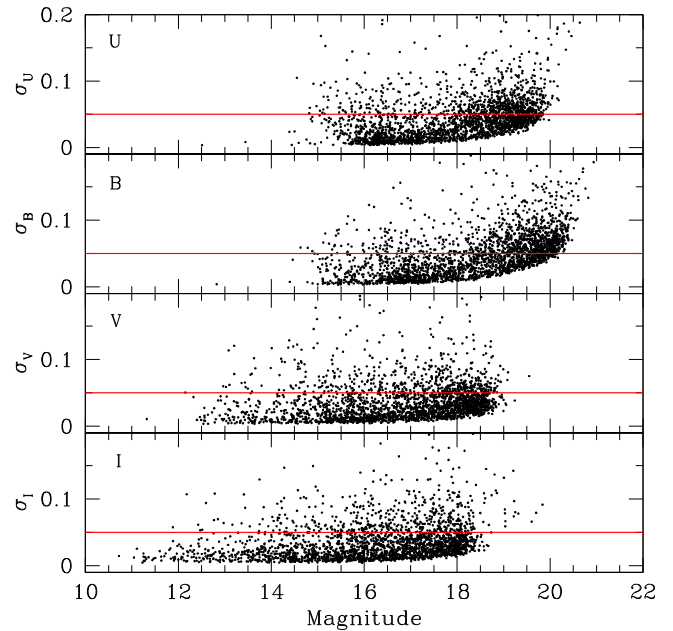


Figure 1. Photometric uncertainty as a function of instrumental magnitude for all stars in our sample. The horizontal red line indicates the cut at 0.05 mag we adopted as our standard cut.

Our results rely on having photometry with very low photometric uncertainties, and the following procedure does not require that the data be transformed to the standard Johnson-Cousins system. Therefore, to avoid introducing added errors the instrumental magnitudes alone were considered sufficient.

Finally, differential reddening is an important consideration when closely examining cluster photometry. In their analysis of differential reddening for 66 Galactic GCs, Bonatto et al. (2013) reported that M13 exhibited minimal differential reddening ($\langle \delta E(B - V) \rangle = 0.026 \pm 0.009$). Given this, we opted to disregard differential reddening as a significant source of dispersion among our M13 sample.

3. Cluster Membership Selection Procedure

To clean the data sets of potential contamination and isolate our final sample of RGB stars, several cuts were instituted. These cuts involved using photometric uncertainty, radial distance from the cluster core, and position on a color–color diagram. Wishing not to bias our results via the quantitative choices we made in these cuts, we also sought to determine the degree to which the overall result was sensitive to some of the adopted cut levels. This validation is described in Section 4.3.

The first cut omitted stars with unacceptably large photometric uncertainty. The literature contains different philosophies on whether such photometric error cuts should be done using a fit to the uncertainty–magnitude plot (e.g., Contreras Peña et al. 2013) or using a fixed value (e.g., Clem et al. 2011), and one can envision scenarios where one or the other approach could be preferred. The sensitivity of our analysis relies upon us using only stars with the best photometry, rather than photometry that is as good as could be expected for a given brightness, so by this rationale we implemented a fixed value cut of 0.05 mag, illustrated for our four filters in Figure 1.

The second cut that was implemented involved radial distance from the cluster center, drawn from Harris (1996).

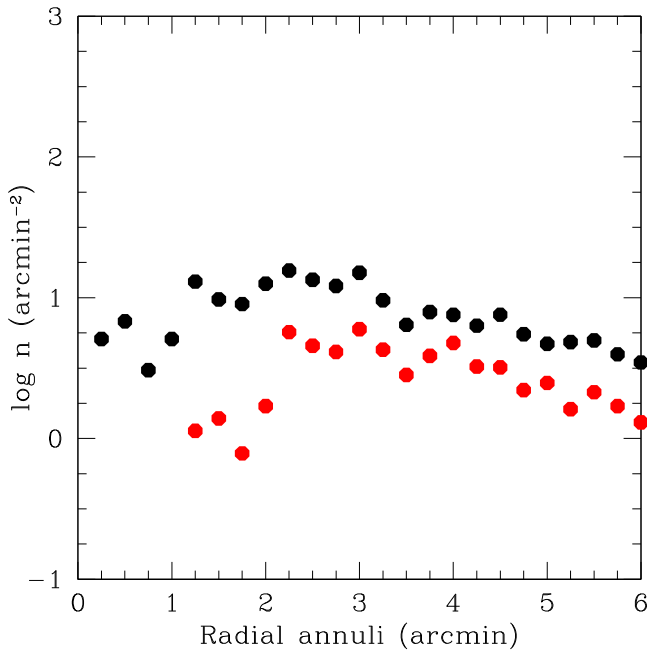


Figure 2. Number density of stars (stars per arcmin²) in our M13 dataset as a function of radial distance from the cluster center. Black data points represent all stars that passed only the uncertainty cut, while red data points represent only the stars that were subsequently used in our multiple population study described in Section 4. Completeness in our final sample begins to drop at a radial distance of approximately 2 arcmin.

To this end, two cuts were implemented for M13: an inner radial cut to avoid stars deemed questionable due to blending, and an outer radial cut to minimize foreground/background contamination. Crowding in the cluster core has a significant impact on ground-based data, leading to a decrease in sample completeness. Figure 2 illustrates the effect of this crowding, where inside 2 arcmin from the cluster center the number density of stars begins to drop off instead of continuing to rise, indicating a decrease in the completeness of our sample. Given this observation, we adopted an inner radial cut of 2 arcmin, which corresponds to 1.2 r_h . An outer radius of 4 r_h was adopted due to the physical limitations of our CCD.

The third cut that was implemented involved removing interloper stars along the RGB. In considering attempts to decontaminate the color–magnitude diagram (CMD) of interloper stars, we utilized the Besançon Galactic model of Robin et al. (2003) to statistically determine the expected number of stars in the direction of M13 that fell along the region of the RGB we ultimately analyzed. We found that the number of contaminating stars on this region of the CMD was minimal (<5), so attempts to statistically decontaminate were omitted. However, omitting foreground/background contamination was necessary to more clearly resolve the RGB for later steps in our procedure. To do this we utilized a quadratic fit to the $(B - V)$ versus $(V - I)$ color–color diagram, shown in Figure 3(a). This color–color combination was chosen because it had both the smallest overall photometric uncertainty and the smallest amount of expected spread resulting from the presence of chemical composition differences among its RGB stars (Sbordone et al. 2011). This fit was subtracted off from the data points and stars within two standard deviations from the mean $\delta(V - I)$ were retained. Results from this were

subsequently compared to results derived from a cutoff at one standard deviation as well.

Stars that passed these cuts were adopted as our candidate cluster members.

4. Distinguishing Multiple Populations

4.1. Review of Prior Methods

The body of literature on identifying MSPs in GCs using ground-based photometry describes approaches that differ to varying degrees. In general, the process involves adopting a fiducial line to represent the shape of the RGB, and then assessing the position of RGB stars in color space with respect to this fiducial line. Some approaches fit such a line to the RGB (e.g., Kravtsov et al. 2010b), others drew such a ridge line in by hand through the RGB (e.g., Monelli et al. 2013, hereafter referred to as Mon13), while still others defined a fiducial line along the edge of the RGB (L11). In any case, the purpose of such a line was to remove the temperature effect from each star’s color and defined a $\delta(\text{color})$ residual as the distance of each star from the adopted fiducial line due to intrinsic chemical differences. Stars at too great a distance from this line, such as horizontal branch (HB) or asymptotic giant branch (AGB) stars or noncluster stars, were removed via some form of a $\delta(\text{color})$ cut. This cut was identified by eye (e.g., Kravtsov et al. 2010b) or statistically (e.g., Mon13).

Distinguishing stellar subgroups visually on a typical CMD is not easy. If spectroscopic data is available, then one can tag stars on a CMD based on their degree of enrichment in key light elements (e.g., Figure 6 in S18). In such instances, individual RGB loci appear largely separated by their degree of enrichment. However, this is not always convenient or possible. To address this, Mon13 defined a new pseudo-color index, $C_{U,B,I} = (U - B) - (B - I)$, in the spirit of Milone et al. (2013), to enhance the impacts that the $(U - B)$ color has in revealing differences in light-element abundance (e.g., Marino et al. 2008) and that $(B - I)$ has in revealing He abundances (e.g., Piotto et al. 2007). On a CMD, this quantity typically reveals multiple loci in the RGB region. S19 used the same $C_{U,B,I}$ definition and visually identified instances where a CMD using this pseudo-color index revealed substructure on the RGB. A similar use of a pseudo-color index was performed by S18 with Strömgen photometry and the index $c_y = (u-v) - (v-b) - (b-y)$ (introduced by Yong et al. 2008). This index also reveals chemical differences among stars on a CMD, in this case differences in N abundance, and results in multiple loci along the RGB that are nearly vertical in y -magnitude along much of the RGB, particularly the lower half. Dividing these multiple RGB loci was then done by drawing a line by hand or fitting a function.

RGB stars within some brightness range were then split into subgroups that were redder or bluer than some criterion. Typically, but not always, that dividing line was the fiducial/ridge line. Some groups (e.g., Kravtsov et al. 2011) identified what we will call a fixed zone of avoidance (ZOA) along the ridge line to omit stars whose uncertainties introduce ambiguity as to which subgroup they belong. Other studies disregarded this step. Cumulative radial distributions (CRDs) of the blue and red subgroups were then examined and quantified using a Kolmogorov–Smirnov (KS) test probability of the two CRDs being drawn from the same parent distribution.

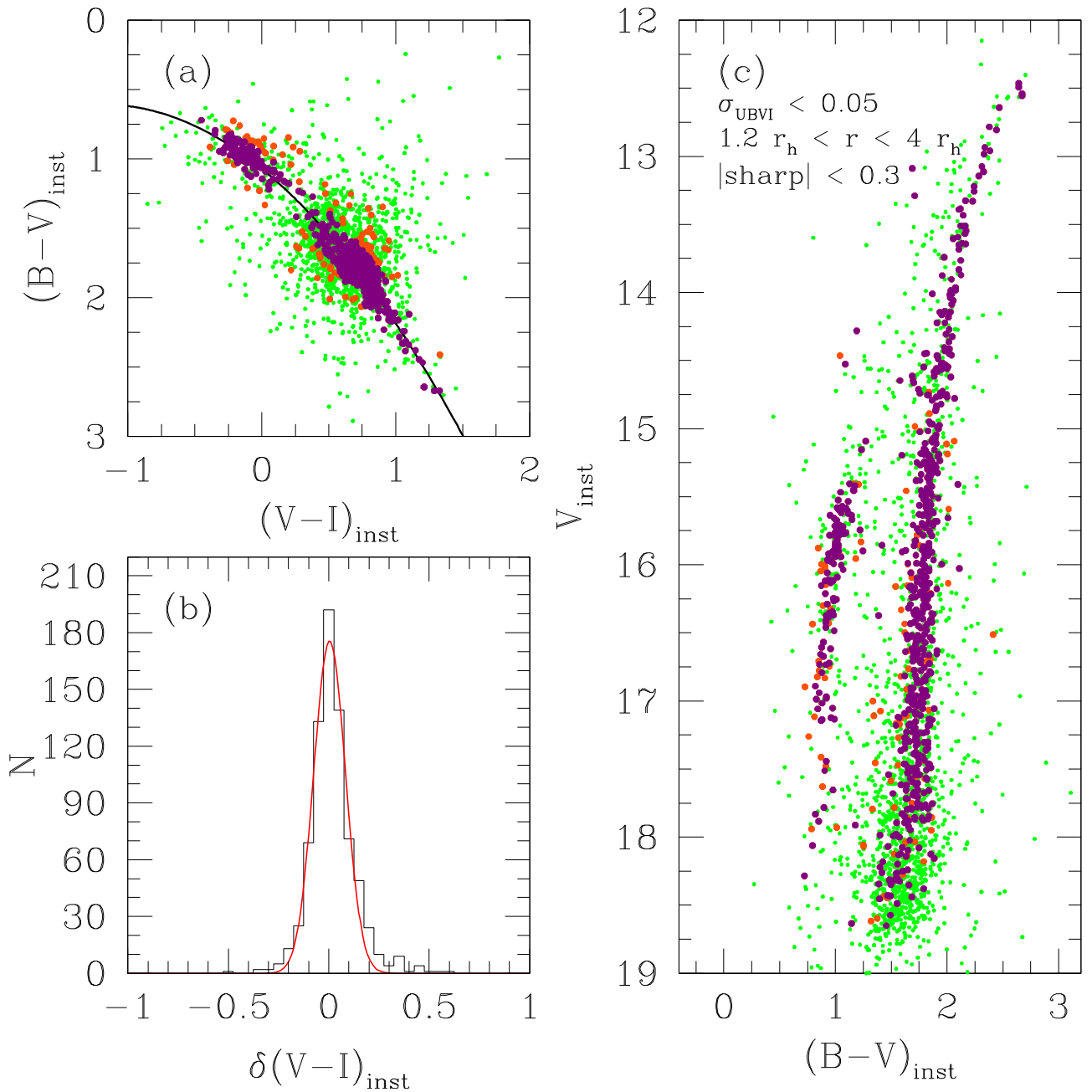


Figure 3. (a): the $(B - V)$ vs. $(V - I)$ color-color diagram for M13. The green points correspond to all stars detected in the field by DAOPHOT, while the orange points correspond to stars remaining after the uncertainty, *sharp*, and radial distance cuts described in the text. A polynomial was fit to these data and subtracted off, resulting in the quantity $\delta(V - I)$. (b): the histogram of $\delta(V - I)$. Stars within 2σ of the mean based on the Gaussian fit shown (red line) were retained and are plotted as purple points throughout this figure. (c): the resulting color-magnitude diagram after this cut, where the purple points were the stars that passed the described cuts and defined our sample of adopted cluster members.

4.2. Our Approach

Figure 4 illustrates our approach in a nutshell. We utilized the $C_{U,B,I}$ definition and examined a CMD showing V -magnitude as a function of $C_{U,B,I}$. Similar to L11 and S18, we isolated a 2.5 mag range along the middle region of the RGB and, noting from Mon13 that this region was not exactly vertical, performed a linear fit to all candidate cluster members along the RGB. This fit served to act as our division between prospective subgroups. While Mon13 claimed to have identified three subgroups in M13, we followed the simpler assumption of two subgroups: one primordial and one enriched in some way. To ascertain the impact of fitting this linear division along

the full RGB, we performed a subsequent test fitting only within the 2.5 mag window as well. It is worth noting that this process assumes the existence of blue and red subgroups on the RGB, which for M13 has previously been demonstrated (e.g. Mon13; S18).

Subtracting off this fit, removing HB stars using a simple color cut, and creating a histogram indicates that while there is no substructure visually apparent on the RGB (see Figure 4(b)), the histogram in Figure 4(c) does provide hints of such overdensities, separated in $\delta C_{U,B,I}$ by an amount comparable to that seen by Mon13. Using the identification of Mon13, we adopted the left side of this histogram as the primordial group

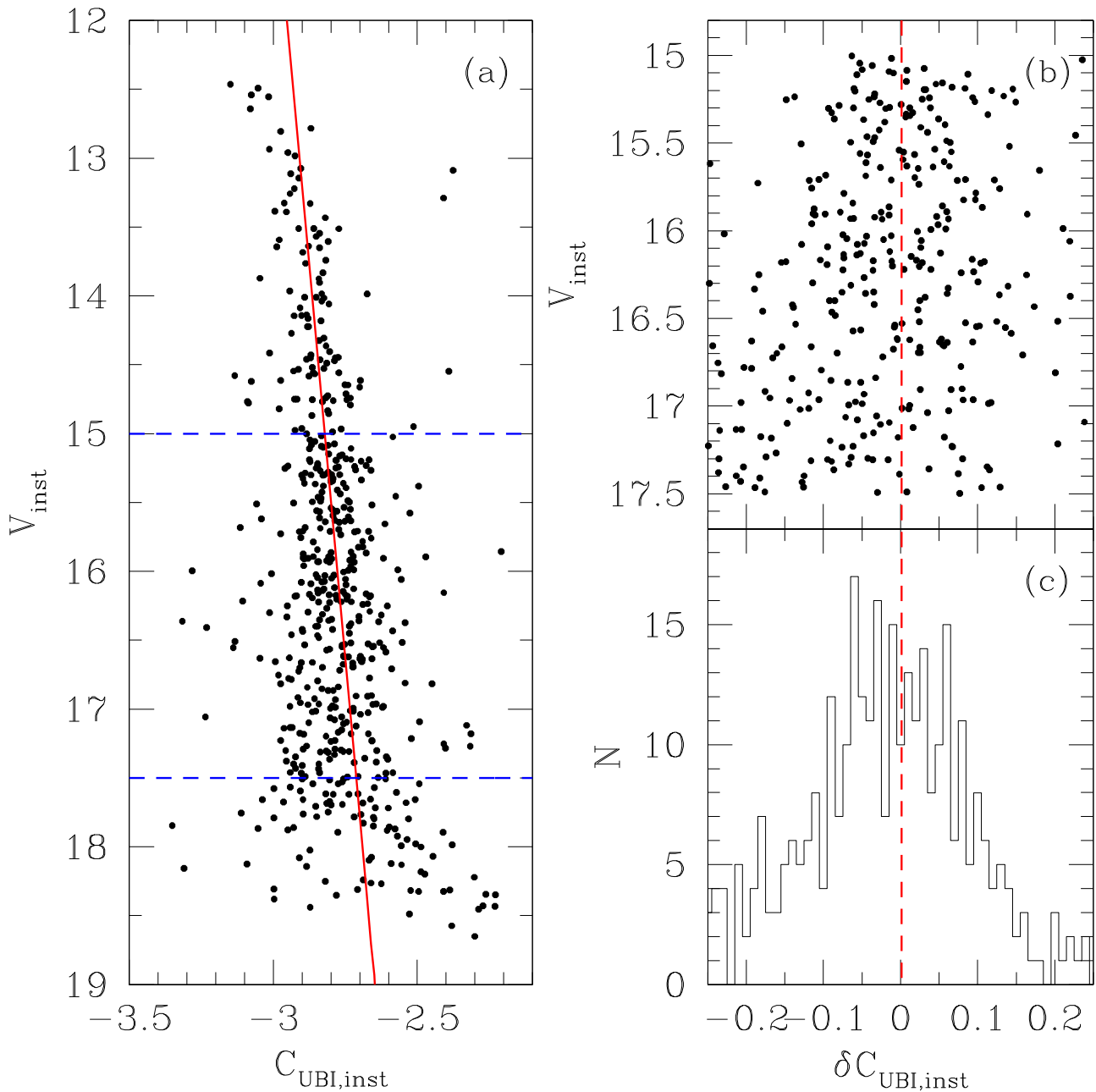


Figure 4. (a): V_{inst} vs. $C_{\text{UBI,inst}}$ for our M13 candidate cluster members. The horizontal blue dashed lines represent the magnitude range used for subsequent steps, chosen to resemble the magnitude ranges used by other studies. The solid red line indicates a linear fit to all of the stars shown in this panel and serves to divide the RGB into two subgroups. (b): the fit-subtracted CMD of all stars shown in (a), but restricted to highlight only the adopted magnitude range. Our dataset does not reveal significant visual indication of distinct subgroup loci due to the relatively small sample size and the impact of scatter that is larger than other studies. (c): the data from (b) in histogram form. There is some suggestion of a meaningful gap in the center that divides two subgroups. This feature was not significantly dependent on bin size and appeared even with bin sizes five times larger or half the size depicted here.

and the right side of this histogram as the enriched group. To avoid the impact of photometric uncertainty on whether a star gets placed in either group, we introduced what we refer to as a dynamic zone of avoidance. In this technique, rather than adopting a fixed-width ZOA as Kravtsov et al. (2011) did we allow each star’s uncertainty in $C_{\text{UBI,inst}}$ to dictate whether it be included or not. If a star’s value of $C_{\text{UBI,inst}} \pm \sigma(C_{\text{UBI,inst}})$ placed it in a position where it could possibly lie on the other side of the midline, that star was omitted.

Mon13 used a limit on $C_{\text{UBI,inst}}$ in order to further eliminate contamination or possible AGB stars by instituting a 5% cut, where the 5% of the reddest and bluest stars in $\delta C_{\text{UBI,inst}}$ were

omitted from consideration at this point. This produced a range in $\delta C_{\text{UBI,inst}}$ of about 0.12 mag in their work. Our scatter is larger than this, where omitting the 5% of the bluest and reddest stars introduces a cutoff at approximately $\delta C_{\text{UBI,inst}} = \pm 0.2$ mag. Panel (a) of Figure 5 illustrates the cumulative radial distributions (CRDs) of the blue (primordial) and red (enriched) subgroups from our sample using the selection process described above, omitting the reddest and bluest 5% of stars. As can be seen, the two distributions do not appear to differ from one another, with the KS probability of being drawn from the same parent distribution at 56%. While we cannot make any claims about the presence or absence of radial

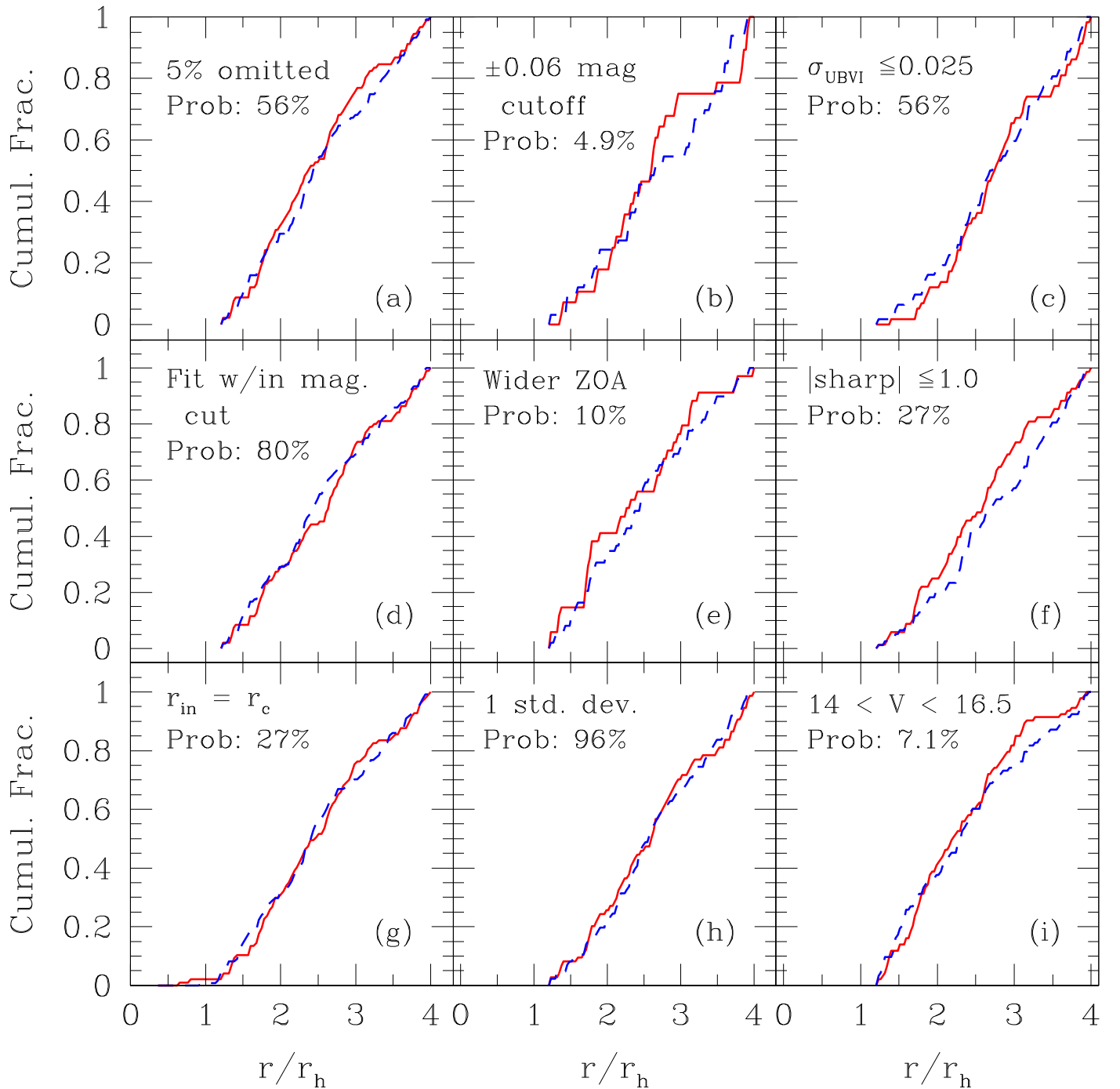


Figure 5. (a): the cumulative radial distribution for the two subgroups of stars selected in Figure 4. The blue (dashed) and red (solid) lines correspond to the subgroups associated with having primordial and enriched chemical abundances, respectively, as identified by Mon13. This represents our standard process. Panels (b)–(i) are the same as (a) but with the following changes: (b): omitting RGB stars at a narrower cutoff range in $\delta C_{U,B,I}$ to reflect the RGB width reported by Mon13; (c): tighter photometric uncertainty cut; (d): fitting the red line in Figure 4(a) only within the adopted 15–17.5 mag range; (e): wider zone of avoidance (ZOA); (f): more generous *sharp* cutoff value; (g): inner radial cut of $1 r_c$; (h): cut of one standard deviation from the mean fit to the $(B - V)$ vs. $(V - I)$ diagram; and (i): magnitude range shifted higher up along the RGB. No meaningful difference between the two distributions is identified in any instance.

concentration among the enriched population outside of $4 r_h$ using our dataset alone, we do conclude that inside $4 r_h$ the two subgroups appear to be dynamically mixed.

4.3. Testing the Impact of Parameter Selection

The process of both producing a sample of candidate cluster members and isolating them into two distinct subgroups involves making certain quantitative choices. In this section

we explore the effect of the particular choices we made by adjusting the values used and examining the impact of those adjustments on the CRDs.

We start by recalling the choice described at the end of Section 4.2 where we adopted a limit on the width of the RGB in $C_{U,B,I}$ space by omitting the reddest and bluest 5% of stars in our sample. This choice could arguably be supported by panel (c) of Figure 4, where the ± 0.2 mag range this introduces does appear to reflect the width of the RGB as seen in our data.

Admittedly, this width is much broader than the width observed by Mon13, so one question is whether or not our results depend on using the RGB width drawn from our own dataset or that of Mon13. To test this, we adopted the width they reported, drawing a ± 0.06 mag cutoff along the fit line. The CRDs associated with this test are shown in panel (b) of Figure 5, along with the corresponding KS probability. The result does not appear to depend on the choice of RGB width.

One might question whether an uncertainty cut of 0.05 mag allows stars with photometric errors into the sample that are too large to be reliable. To this end, we explored the effect of decreasing the limit to 0.025 mag, shrinking the number of stars but retaining only those with the best measurements. Panel (c) in Figure 5 illustrates the new CRDs, which are again statistically indistinguishable from one another.

In Figure 4 we showed the linear fit to the $C_{U,B,I}$ RGB using all stars in that sample. It is reasonable to check whether this is the best approach, given that the bright tip of the RGB exhibits a curve in the results reported by Mon13. For this reason, we tested a linear fit using only RGB stars in the magnitude range we adopted. The CRDs produced by the subgroups defined by this fit are shown in Figure 5(d).

We also consider the impact of the possibility that our photometric uncertainties are underestimated. In such a case, the dynamic ZOA we allowed in our standard procedure may not be large enough to assure that stars on the red side of the midline are indeed redder than average. To accommodate this possibility, we explored widening the ZOA to ± 0.1 mag, ~ 10 times our mean uncertainty. Figure 5(e) illustrates the CRDs from such an adjustment. ZOA widths of ± 0.05 and ± 0.075 yielded identical results.

Panel (f) in Figure 5 illustrates the impact of increasing our *sharp* limit, allowing more stars into the sample that have slightly less star-like light profiles. The result is unchanged. Not shown here is an additional test we performed by shrinking the limit on *sharp* to 0.2, restricting the sample to stars with even more star-like light profiles. Again, the result was not affected.

It is typical to consider making an inner radial cut with ground-based photometry, as seeing will introduce a limit to how well the innermost regions of GCs can be resolved. Given its relatively large angular size and brightness, resolving stars inside $1 r_h$ may be conceivable if the observing site and conditions are optimal along with a high S/N. Our standard procedure described above adopted an inner radius cut of $1 r_h$ to align it with the studies we use for comparison, namely L11 and S18 who also adopted inner radial limits of $\approx 1 r_h$ for their ground-based M13 data. However, L11 actually uses a somewhat smaller inner radial cut of $0.7 r_h$, which while not terribly different does probe deeper into the cluster center. Given this fact, and the significance of their conclusion, we explored what our own CRDs would look like if we too probed deeper toward the cluster center. Panel (g) in Figure 5 indicates the resulting population distribution for an adopted inner radius cut of $1 r_c$, which corresponds to approximately $0.4 r_h$ (Harris 1996). As can be seen, the other cuts we utilized remove most of the stars inside $1 r_h$ within our sample already so decreasing the inner radial limit does not impact our result.

When performing the fit to the color-color diagram shown in Figure 3(a) we accepted stars that fell within 2σ of the mean fit. To explore the impact of this choice, we ran a test restricting the window of acceptance to just 1σ . The result is shown in

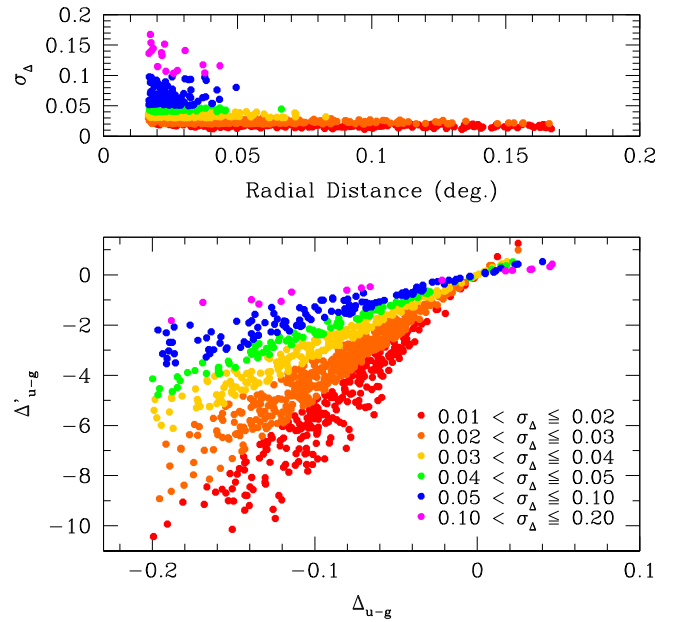


Figure 6. Top panel: photometric uncertainty in the Δ_{u-g} color differential adopted by L11 as a function of radial distance from the cluster center. Bottom panel: the normalized color differential Δ'_{u-g} derived by L11 as a function of the original Δ_{u-g} value, colored according to the photometric uncertainty in Δ_{u-g} . While all values of σ_{u-g} exist over the full range of Δ_{u-g} , after the normalization the stars with larger σ_{u-g} preferentially reside at redder values of Δ'_{u-g} .

panel (h) of Figure 5, and it can be seen that the result is the same.

Finally, panel (i) in Figure 5 addresses the possibility that we are avoiding a significant red population in the cluster that has higher luminosity than our bright limit. The bright limit in the L11 sample from SDSS lies somewhat higher up on the RGB, so we tested our sample by shifting the 2.5-mag-wide brightness window up to span the range $14 \leq V_{inst} \leq 16.5$. Regardless of whether or not we opted to perform the linear fit to the RGB within this new magnitude range, the KS probability remained essentially unchanged.

The similarity of these diagrams and relatively high KS probabilities indicate that our result is independent of the parameter choices we made. We conclude that through rigorous testing of our cut parameter choices, we consistently obtain the result that inside $4 r_h$ M13 appears to be well mixed.

5. Resolving the Conflict

The radial distributions of subpopulations in M13 have been studied previously by L11 and S18, with conflicting results. The procedures and data sets they used have both similarities and differences. The two ground-based data sets from both studies were obtained using comparable instruments, have comparable seeing limits and photometric errors, were both measured using the DAOPHOT suite, and span nearly identical radial distance ranges. It seems safe to conclude that the two data sets are of equal or comparable quality overall.

Both procedures involved adopting a fiducial line that allowed the photometry to be separated into red and blue subgroups. Strömgren photometry using appropriate pseudo-color indices has been shown to serve as an excellent tool for separating out chemically different subpopulations, exceeding that of SDSS ($u - g$) alone as used by L11. On the other hand,

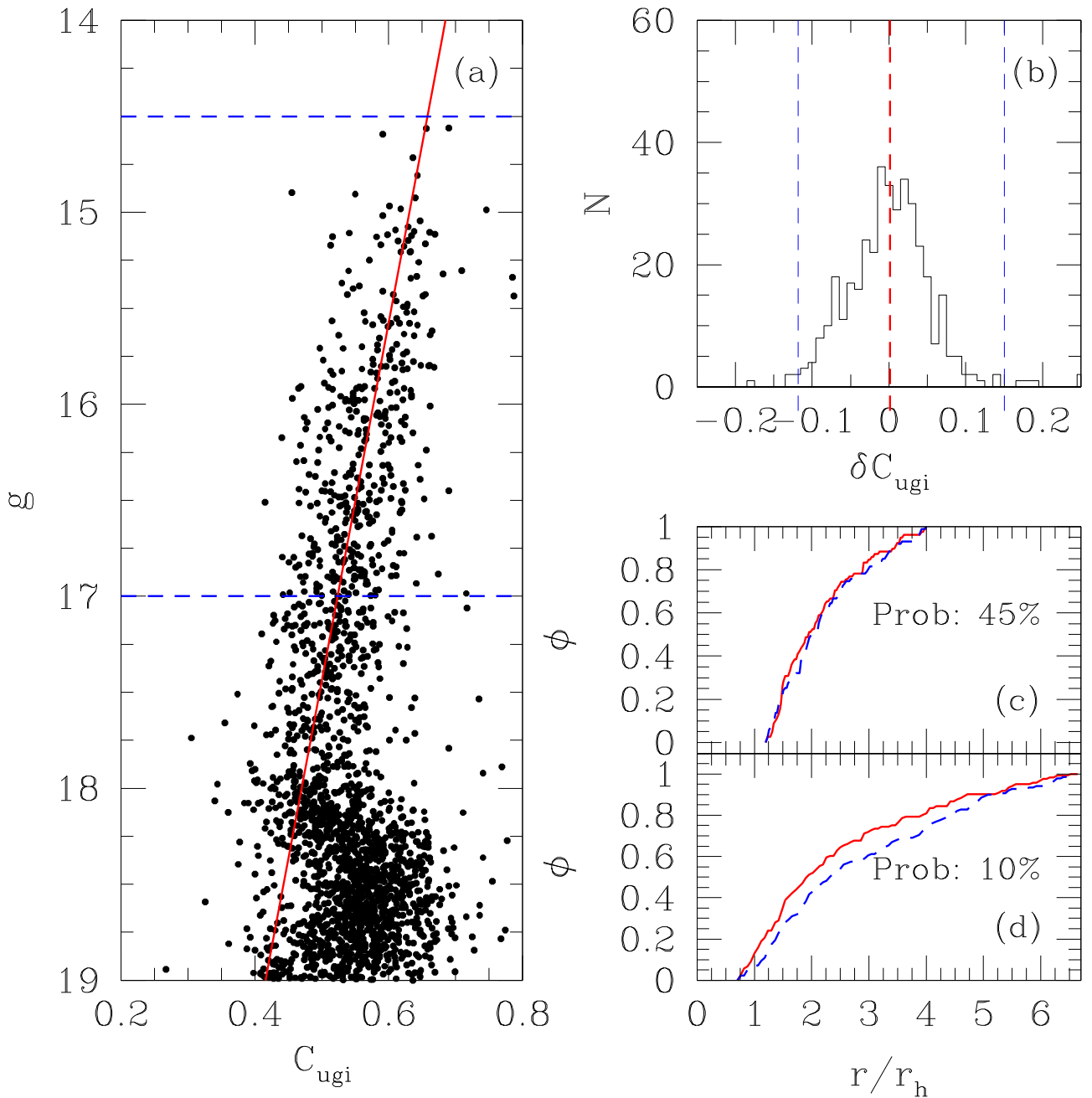


Figure 7. Similar to Figure 4, where panels (a) and (b) correspond to panels (a) and (c) in Figure 4, respectively, but from the SDSS dataset used by L11 over the radial range of 1–4 r_h . Again, the horizontal blue dashed lines in (a) indicate the magnitude range used, and the vertical blue dashed lines in (b) indicate the cut made by omitting the extreme 5% of the sample. (c) and (d): CRDs for our process applied to the SDSS dataset, with distance ranges of 1–4 r_h and 0.7–6.7 r_h , respectively. The central concentration vanishes in these CRDs, with KS tests being 35% and 34%, respectively.

broadband ($U - B$) has been shown to have some success and it is not obvious that ($u - g$) should suffer compared to this. It seems reasonable, then, to conclude that it ought to be possible to separate chemically different subgroups using ($u - g$) if the procedure is applied carefully.

The fundamental difference between the two procedures described by L11 and S18 is how photometric uncertainty was handled. S18 proceeded with a cut on photometric uncertainty, rejecting stars outside three standard deviations from the mean uncertainty at a given magnitude in all filters. This has the effect of retaining stars that are measured as well as could be expected for their brightness. Although this could, in principle, lead to the inclusion of stars with objectively large uncertainty,

the magnitude range they ultimately used for the study omitted stars with that concern.

On the other hand, L11 did not cut by photometric uncertainty. Instead, once they had their color differentials Δ_{u-g} (the color difference between each star and the adopted fiducial line) they divided these values by the color uncertainty σ_{u-g} , with the assumption that this normalization accounts for the uncertainty contribution by “dividing it out,” producing a Δ'_{u-g} value that is presumably uncertainty-accommodated.

We reprocessed the L11 data to investigate the impact of this approach using the procedural details the authors described as closely as possible. In the bottom panel of Figure 6 we see that over the full range of the original Δ_{u-g} there are stars with

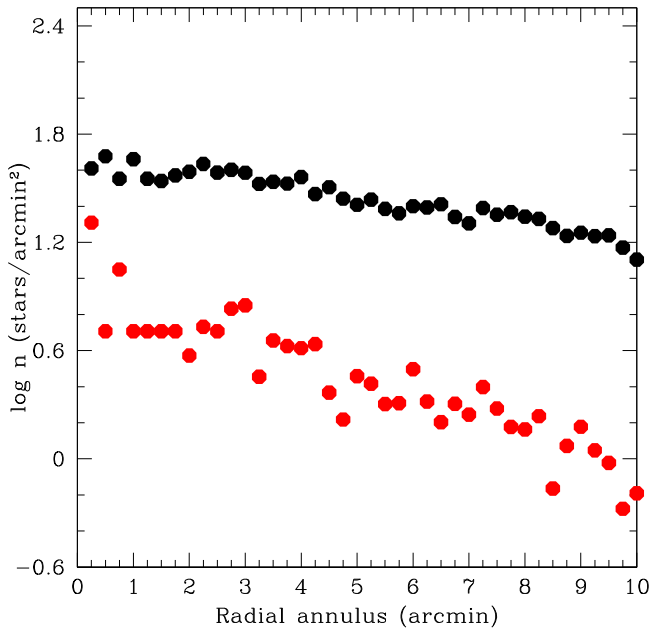


Figure 8. Same as Figure 2, but for the M13 photometry from S19.

small and large uncertainties, as expected. Once this normalization $\Delta'_{u-g} = \Delta_{u-g}/\sigma_{u-g}$ is performed, though, the stars with large photometric errors preferentially reside on the red end of the new Δ'_{u-g} distribution. As can be seen, stars with red Δ_{u-g} values remain on the red end of the Δ'_{u-g} distribution, regardless of their photometric uncertainty. Normalizing does nothing to allow these stars to shift to the blue side. Stars with blue Δ_{u-g} values can shift due to this normalization, and the effect is to preferentially move bluer stars with large uncertainties back toward the red end in Δ'_{u-g} . The top panel of Figure 6 shows that stars with the largest uncertainty in Δ_{u-g} reside closer to the cluster center. It seems possible to conclude, then, that the centrally concentrated red (Δ'_{u-g}) subgroup identified by L11 may have simply been the result of a bias in how the photometric uncertainty was addressed.

To verify that our suspicion is not unfounded, we applied our standard procedure described in Section 4.2 to the L11 M13 data drawn from SDSS, following the approach described by An et al. (2008) with respect to determining an overall value of the DAOPHOT *chi* and *sharp* values for quality control purposes. Following our procedure required consideration of the $C_{U,B,I}$ index adopted earlier and how the SDSS filters compare. We are unaware of any rigorous attempts to test and define a similar index in the SDSS filter system. Given the spectral coverage of the SDSS filter set compared to the Johnson-Cousins system, it seems like a reasonable approximation to define an analogous pseudo-color $C_{u,g,i} = (u-g) - (g-i)$ and we will proceed using this index with the assumption that while it carries a degree of uncertainty about whether or not it is the most appropriate pseudo-color in the SDSS filter set, it is unlikely to be the worst, nor likely to be entirely inappropriate for our purpose.

Figure 7 illustrates the RGB of M13 in this SDSS pseudo-color. We again adopt a 2.5-mag-wide range, which is composed of the entire magnitude range L11 adopts along with an additional half-magnitude on the bright end. We then examined CRDs over the radial range of $1.2\text{--}4 r_h$ (Figure 7(c)) for comparison with our results using other data sets, and over

$0.7\text{--}6.7 r_h$ (Figure 7(d)) to compare with the results reported by L11. In both cases, the central concentration of red RGB stars appears to have vanished based on visual inspection as well as consideration of the KS probabilities, supporting the idea that how one chooses to address photometric uncertainty in this type of analysis is of paramount importance.

6. Dynamical Mixing Expectations

Given the discrepancy of prior published results, examining the dynamical predictions should provide insightful expectation regarding the radial distribution of the two populations. Simulations of GC dynamics in the context of the formation of multiple populations are abundant, and generally these simulations predict that any subsequent generation of stars that form after the cluster initially forms should be centrally concentrated at first. The cluster then evolves through multiple dynamical mechanisms such that over time the new population (s) become increasingly mixed throughout the primordial population.

Dalessandro et al. (2019) reported on the results of N -body simulations that began with centrally concentrated second populations and thereafter evolved over a large number of dynamical timescales. During these simulations, they tracked the disparity between the radial distributions of the first and second populations, defining this difference using the parameter A^+ , where

$$A^+(R) = \int_{R_{\min}}^R (\phi_{FP}(R') - \phi_{SP}(R')) dR'. \quad (1)$$

This corresponds to the area enclosed between the CRDs of the two subpopulations, where *FP* and *SP* indicate the first (primordial) population and the second (enriched) population, respectively. A strongly centralized second population results in negative values of A^+ , which they showed then evolve toward zero over time as the two populations mix. In their simulations, they only considered the innermost $2 r_h$, thus dubbing their parameter A_2^+ .

While our own dataset does not include the innermost $1 r_h$, there is a dataset that does. Stetson et al. (2019, hereafter referred to as S19) presented the public release of an extensive database of ground-based photometry for globular and open star clusters. We obtained the *UBVI* dataset for M13 and again examined the dataset for completeness issues in the inner regions due to crowding. Figure 8 indicates that beyond 2 arcmin the data appears to behave as expected, while inside 2 arcmin it is less obvious that the dataset is complete. We applied the standard procedure described above to select the subset of candidate cluster members illustrated in panels (a) and (b) of Figure 9. We first examined the same radial distance range as we did for our own dataset to determine whether or not our result depended on our dataset. Figure 9(c) shows that this is not the case—both our dataset and the S19 dataset, undergoing the same procedure over the same radial range with all other cuts being the same, reveal what looks like a well-mixed distribution of stars.

Having established confidence in our procedure, we then turned our attention to the inner $2 r_h$ (3.4 arcmin) in the S19 dataset. We re-ran the selection and division process that extracted out the primordial and enriched subgroups within the $0\text{--}2 r_h$ range this time (shown in Figure 9(d)). Again, we see (not surprisingly) that the two populations are generally well mixed inside $2 r_h$ as well. Finally, we examined the radial range

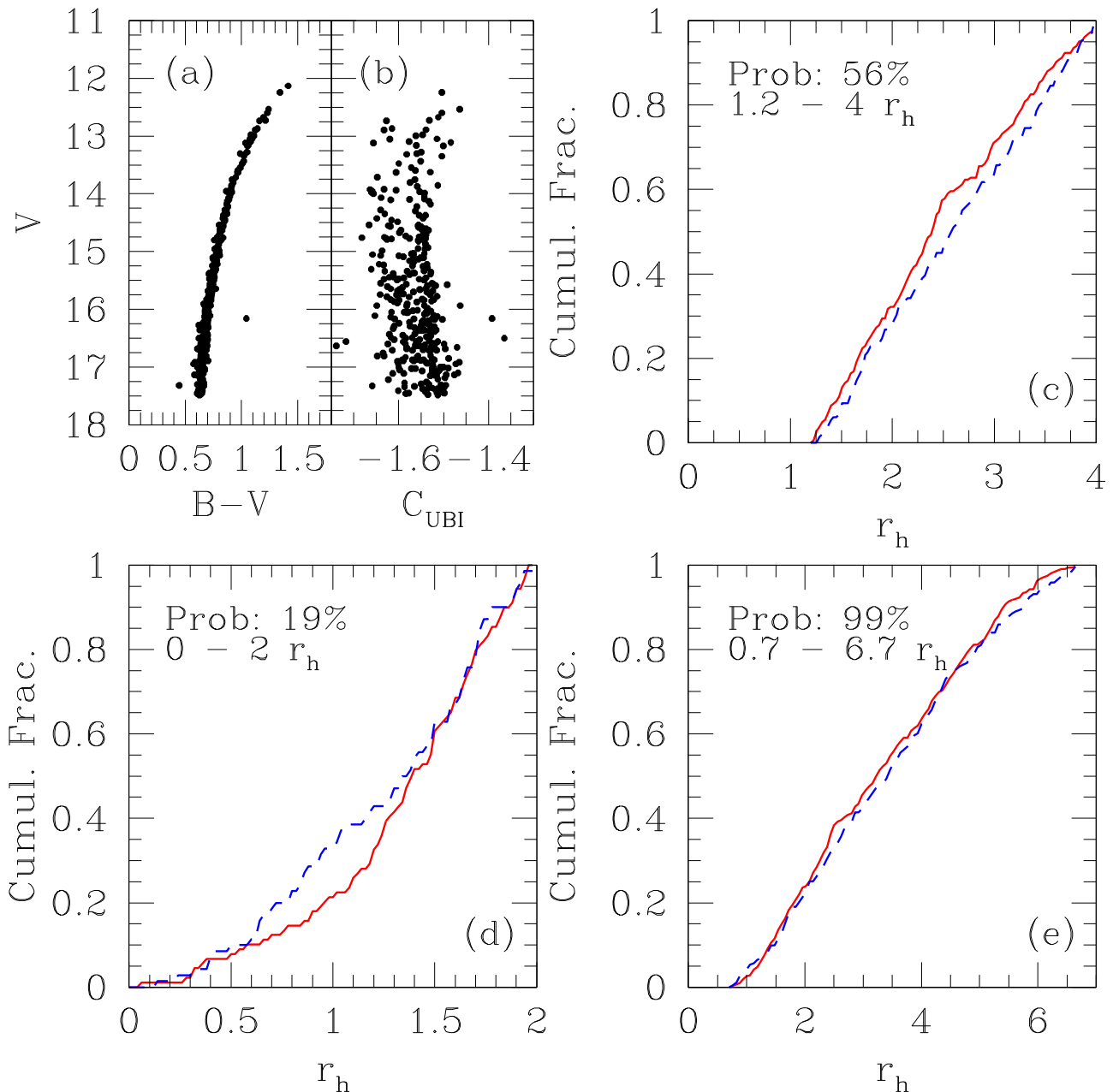


Figure 9. (a): CMD of M13 from S19 illustrating the candidate cluster RGB stars only. (b): CMD of M13 shown in $C_{U,B,I}$ space. (c)–(e): CRDs of red (solid red line) and blue (dashed blue line) RGB stars over the radial distance ranges shown. KS probabilities for each CRD are shown, emphasizing the similarity between the two subgroups over each radial range.

covered by Mon13, L11, and S18 using the S19 archive photometry over the specific radial range used by L11 and see, as shown in Figure 9(e), that the cluster appears well mixed throughout.

From the CRDs shown in panel (d) of Figure 9, we could potentially calculate a value of A_2^+ for comparison with the results from Dalessandro et al. (2019). Doing so depends on the dataset being complete over this radial range or that the region where it is incomplete is sufficiently well mixed that there is no difference between the radial distributions of the enriched and unenriched subgroups. While the number density of stars in Figure 8 over this radial range does not smoothly follow the overall trend inside 2 arcmin, it also does not drop precipitously

as our data did in Figure 2. It is tantalizing enough that we pursued the option, arriving at a value of $A_2^+ = 0.002$. Using M13’s published age of 11.65 Gyr (Forbes & Bridges 2010, and references therein) and the dynamical time of $t_{rh} = 1.995$ Gyr from Harris (1996), we were able to place M13 on the simulation results of Dalessandro et al. (2019), shown in Figure 10. These results appear to illustrate that not only does M13 seem well mixed inside $2 r_h$, but that this observation appears consistent with dynamical predictions (notwithstanding our assumption that the data are relatively complete inside 2 arcmin). This supports the further observation from the S19 dataset, and our own, that M13 also appears to be well mixed out to at least $6.7 r_h$.

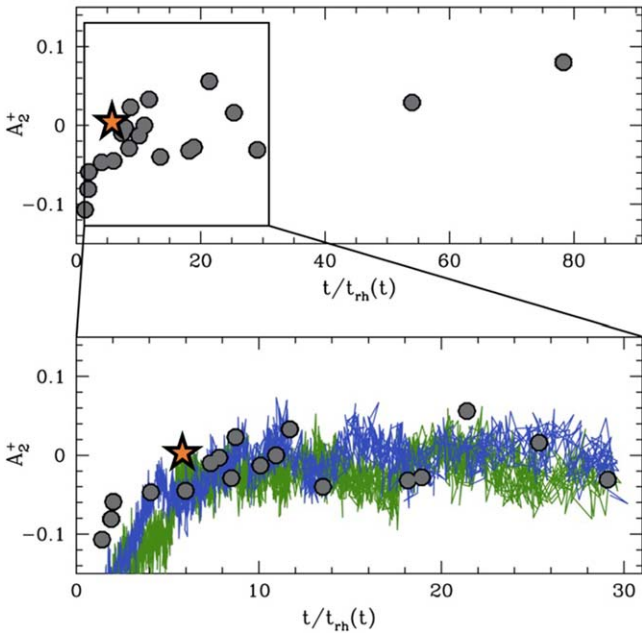


Figure 10. Reproduction of Figure 3 from Dalessandro et al. (2019), illustrating the distribution of A_2^+ values drawn from their cluster sample (top panel) and overlaid onto N -body simulations (bottom panel). Our data point for M13, drawn from the analysis of the S19 data, is overlaid onto both panels as an orange star. The placement of the orange star is consistent within the scatter illustrated by their simulations. (Reproduced by permission of the author and AAS).

7. Conclusion

In this work we addressed an apparent conflict in the literature between L11 and S18 regarding the nature of the radial distributions of chemically distinct subgroups within the Galactic GC M13. Visually distinguishing separate populations on the RGB is difficult for all but the best photometry, but it has been shown that the $C_{U,B,I}$ color index provides an optimal separation between the two populations. We proceeded to use this color index to cut our sample of stars down to stars very likely to be cluster members and divided that sample into known enriched and primordial subgroups guided by the results of Mon13 for M13. Cumulative radial distributions of the two subpopulations appear to be consistent with having been drawn from the same overall distribution.

To demonstrate the veracity of our result we first rigorously tested our approach by selecting reasonable alternative values for our cut criteria. Notably, we considered the possibility that our data may be affected by underestimated photometric uncertainty by defining different zones of avoidance around the RGB midline, to assure ourselves that we were only considering stars that were truly redder or bluer than average. Second, we used archival data assembled by S19 to assess whether our dataset alone might be at all responsible for our result. Finally, we repeated our procedure on the SDSS dataset used by L11. In all cases, cumulative radial distributions and KS probabilities supported the conclusion that M13 is well mixed out to a radial distance of approximately $7 r_h$ from the cluster center. This observation using RGB stars supports the observation of Vanderbeke et al. (2015), in addition, who traced the populations using HB stars in M13 and also found them to be well mixed.

We believe the source of the apparent conflict found in the literature regarding the dynamical state of M13 stems from the method L11 adopts to account for the photometric uncertainty in

the SDSS dataset. The normalization process they describe appears to introduce a bias that preferentially moves stars with large uncertainties from the bluer side of the RGB to the redder side. Since stars with larger uncertainties are preferentially located near the center of the cluster, the result is an apparent central concentration of redder stars. In a future paper (in preparation), we will present the results of a re-analysis of the other clusters in L11. Finally, the consistency among the results drawn from our own data, the S19 archive, and the SDSS data also suggests that if there are no significant limitations to available exposure time, modestly sized telescopes have the potential to make meaningful contributions to this type of research.

J.P.S., W.B.H., A.J.V., and Z.J.B. acknowledge partial support from the Michigan Space Grant Consortium and the Calvin Research Fellowship program. Students W.B.H., A.J.V., and Z.J.B. are grateful for additional support from the Kanis, John Van Zytveld, and Hubert A. Vander Plas Memorial summer student research fellowships. This research was also made possible by supporting funds from the Calvin University Science Division. Finally, we are indebted to Peter Stetson, Deokkeun An, Charles Kuehn, and Nathan De Lee for advice and guidance with DAOPHOT, and Charles Bonatto for providing us with a differential reddening map of M13 for reference. We also appreciate the helpful feedback from the referee.

Software: DAOPHOT (Stetson 1987).

ORCID iDs

Jason P. Smolinski <https://orcid.org/0000-0002-2045-7353>
 Alex J. Van Kooten <https://orcid.org/0000-0002-3905-4853>
 Peyton Benac <https://orcid.org/0000-0002-9384-5365>

References

- Abazajian, K. N., Adelman-McCarthy, J. K., Agüeros, M. A., et al. 2009, *ApJS*, **182**, 543
- An, D., Johnson, J. A., Clem, J. L., et al. 2008, *ApJS*, **179**, 326
- Bastian, N., Cabrera-Ziri, I., & Salaris, M. 2015, *MNRAS*, **449**, 3333
- Bonatto, C., Campos, F., & Kepler, S. O. 2013, *MNRAS*, **435**, 263
- Carretta, E., Bragaglia, A., Gratton, R. G., et al. 2010, *A&A*, **516**, A55
- Clem, J. L., Landolt, A. U., Hoard, D. W., & Wachter, S. 2011, *AJ*, **141**, 115
- Contreras Peña, C., Catelan, M., Grundahl, F., Stephens, A. W., & Smith, H. A. 2013, *AJ*, **146**, 57
- Dalessandro, E., Cadelano, M., Vesperini, E., et al. 2019, *ApJL*, **884**, L24
- Forbes, D. A., & Bridges, T. 2010, *MNRAS*, **404**, 1203
- Harris, W. E. 1996, *AJ*, **112**, 1487
- Kravtsov, V., Alcaíno, G., Marconi, G., & Alvarado, F. 2010a, *A&A*, **516**, A23
- Kravtsov, V., Alcaíno, G., Marconi, G., & Alvarado, F. 2010b, *A&A*, **512**, L6
- Kravtsov, V., Alcaíno, G., Marconi, G., & Alvarado, F. 2011, *A&A*, **527**, L9
- Lardo, C., Bellazzini, M., Pancino, E., et al. 2011, *A&A*, **525**, A114
- Larsen, S. S., Baumgardt, H., Bastian, N., et al. 2015, *ApJ*, **804**, 71
- Lim, D., Lee, Y.-W., Pasquato, M., Han, S.-I., & Roh, D.-G. 2016, *ApJ*, **832**, 99
- Marino, A. F., Villanova, S., Piotto, G., et al. 2008, *A&A*, **490**, 625
- Milone, A. P., Marino, A. F., Piotto, G., et al. 2013, *ApJ*, **767**, 120
- Monelli, M., Milone, A. P., Stetson, P. B., et al. 2013, *MNRAS*, **431**, 2126
- Piotto, G., Bedin, L. R., Anderson, J., et al. 2007, *ApJL*, **661**, L53
- Piotto, G., Milone, A. P., Bedin, L. R., et al. 2015, *AJ*, **149**, 91
- Robin, A. C., Reylé, C., Derrière, S., & Picaud, S. 2003, *A&A*, **409**, 523
- Savino, A., Massari, D., Bragaglia, A., Dalessandro, E., & Tolstoy, E. 2018, *MNRAS*, **474**, 4438
- Sbordone, L., Salaris, M., Weiss, A., & Cassisi, S. 2011, *A&A*, **534**, A9
- Stetson, P. B. 1987, *PASP*, **99**, 191
- Stetson, P. B., & Harris, W. E. 1988, *AJ*, **96**, 909
- Stetson, P. B., Pancino, E., Zocchi, A., Sanna, N., & Monelli, M. 2019, *MNRAS*, **485**, 3042
- Vanderbeke, J., De Propris, R., De Rijcke, S., et al. 2015, *MNRAS*, **451**, 275
- Yong, D., Grundahl, F., Johnson, J. A., & Asplund, M. 2008, *ApJ*, **684**, 1159